JOURNAL OF APPLIED PHYSICS **101**, 064305 (2007)

Modeling and simulation of axisymmetric coating growth on nanofibers

K. Moore, C. B. Clemons, K. L. Kreider, and G. W. Young[a]
Department of Theoretical and Applied Mathematics, University of Akron, Akron, Ohio 44325-4002

(Received 7 September 2006; accepted 12 January 2007; published online 21 March 2007)

This work is a modeling and simulation extension of an integrated experimental/modeling investigation of a procedure to coat nanofibers and core-clad nanostructures with thin film materials using plasma enhanced physical vapor deposition. In the experimental effort, electrospun polymer nanofibers are coated with metallic materials under different operating conditions to observe changes in the coating morphology. The modeling effort focuses on linking simple models at the reactor level, nanofiber level, and atomic level to form a comprehensive model. The comprehensive model leads to the definition of an evolution equation for the coating free surface. This equation was previously derived and solved under a single-valued assumption in a polar geometry to determine the coating morphology as a function of operating conditions. The present work considers the axisymmetric geometry and solves the evolution equation without the single-valued assumption and under less restrictive assumptions on the concentration field than the previous work. © *2007 American Institute of Physics*. [DOI: 10.1063/1.2710442]

I. INTRODUCTION

The coating of nanoscale structures and the evolution of crystalline structure at the nanoscale are and will continue to be important issues. This article is a continuation of Refs. 1 and 2. Those works presented a coordinated experimental and modeling program for the synthesis of core/clad and hollow nanowire structures. Physical vapor deposition techniques were used to apply coatings to electrospun polymer nanofibers. These fibers were coated with films of copper, aluminum, titanium, zirconium, and aluminum nitride by using a plasma enhanced physical vapor deposition (PEPVD) sputtering process, as shown in Fig. 1.

For reference, some details of the reactor and the synthesized nanowires are described. In the reactor, a power supply drives a 2 in. diameter electrode that forms the target (or source) material. A mat of nanofibers is placed on a holder that sits 8 cm above the target. When a negative electrical potential is applied to the electrode (target), a plasma of positively charged ions forms in the gas phase. The resulting electric field causes these ions to impact the target. These collisions, in turn, sputter neutral species of the target material into the gas phase. Once in the gas phase, the neutral species are transported throughout the reactor and are deposited on all available surfaces, including the nanofibers. Ions from the plasma also strike the coated nanofibers, but typically with much less energy because the substrate is not biased. These collisions tend to smooth out the coating through a resputtering process. The coating growth rate depends on the rate at which atoms are supplied to the nanofiber surface, the nanofiber temperature, and the ion flux to the nanofiber. The morphology of the coating depends on the mobility of the atoms on the surface and how much time the atoms have to move around before the next atoms hit the surface. The rate at which atoms are supplied to a nanofiber is proportional to the rate at which atoms are sputtered from the target and how far away the nanofiber is from the target. The sputtering rate depends on the ion flux, which is determined by the power applied to the target, the pressure of the system, and the working gas used.[3]

Transmission electron microscopy (TEM) is used to determine the effects of these variables on the film growth rate and morphology. The average thicknesses of the fibers before and after the coating process are compared to determine an average growth rate of the fibers. To determine coating morphology and crystalline structure, TEM images and diffraction patterns are taken.

Figures 2(a)–2(c) show nanofibers coated with aluminum. Following deposition, the polymer nanofiber may be removed by pyrolisis while leaving the coating. The approximate thickness of the coating was controlled by the sputtering process. Figures 2(a)–2(c) show that different coating morphologies, nodular versus wavy, are obtained. The origin of these morphologies is unclear. From Figs. 2(b) and 2(c) it appears that the wavelength of the coating in the axial direction is larger for larger diameter fibers.

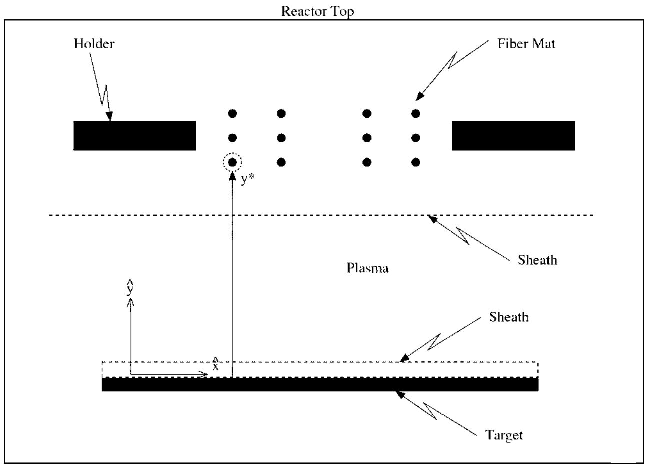

FIG. 1. Global schematic of the reactor for neutral species transport within the reactor (not drawn to scale or proportion).

---

[a] Electronic address: gwyoung@uakron.edu

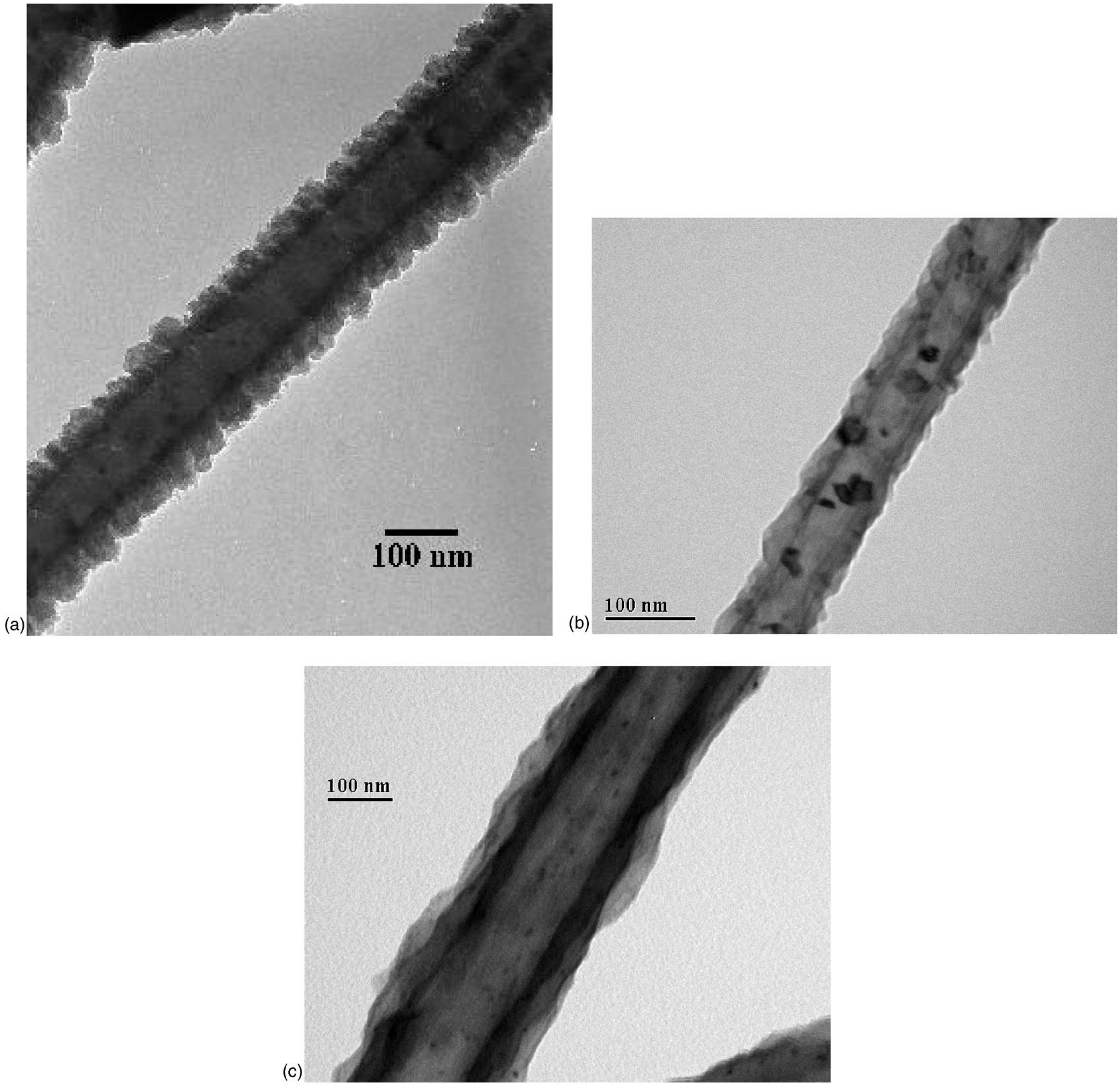

FIG. 2. TEM images of aluminum-coated nanofibers. (a) Nodular coating morphology. (b) Wavy coating morphology on a small radius nanofiber. (c) Wavy coating morphology on a large radius nanofiber.[15]

The approach described above can be used to produce cylindrical, multilayered, nanostructures with precisely controlled interfaces composed of many materials including metals, semiconductors, ceramics, and polymers with controlled diameters and a range of nanometer thickness walls.

II. OVERALL MODELING APPROACH

To aid the understanding of the deposition process on nanoscale size structures, a comprehensive model for the coating of nanofibers within a traditional PEPVD system is described in Refs. 1 and 2. The model integrates across atomic to continuum length scales for simulating the sputtering, transport and deposition of coating material onto a nanoscale substrate. The model connects macroscale phenomena to nanoscale phenomena by linking simple models at each length scale. The solution procedure involves many simplifying assumptions to piece together a collection of simple models into one comprehensive model. Solution strategies that couple continuum and atomistic models are used. Information is passed between the various length scale models so that the simulations are integrated together. To keep the numerical simulations at a manageable level, asymptotic analyses are used to reduce the complex models to simpler, but still relevant, models. The intent of the present paper is to enhance the submodel for the transport and deposition local to the nanofiber.

In Part I of this series, we describe a continuum model of the sheath region at the target and the reactor dynamics near the target surface.[1] At the atomic level, we use molecular dynamics (MD) simulations to study the sputtering and deposition mechanisms at the target. Ion kinetic energies and fluxes are passed from the continuum sheath model to the MD simulations. These simulations calculate sputtering and sticking probabilities that in turn are used to calculate parameters for the continuum reactor model. The reactor model determines the concentration of the coating material.

In Part II of this series we describe the sheath region at the holder and the local dynamics near the substrate surface.[2] The concentration from Part I is input to this local model. At the atomic level, we use MD simulations to study the sputtering and deposition mechanisms at a curved surface. Ion kinetic energies and fluxes are passed from the continuum sheath model to these MD simulations. These simulations calculate sputtering and sticking probabilities that in turn are used to calculate parameters for the local model. The local model determines an evolution equation for the coating surface. A polar geometry is assumed for the coating surface. In deriving the evolution equation, we assume two levels of simplification to derive the concentration field of the coating material. First, the concentration field is assumed to be radially dominant and so variations in the angular direction are neglected. This leads to a concentration field that depends highly nonlinearly on the location of the coating surface. Hence, a second simplification is posed. The location of the coating surface is replaced by the radius of the uncoated nanofiber. Finally, the coating surface is assumed to be single valued so that coating morphologies such as those in Fig. 2 are excluded from consideration. These simplifications reduce the complexity of the numerical simulation of the evolution equation. Nevertheless, parametric studies of this evolution equation reveal general trends that rougher coatings develop on nanofibers with larger radii, in systems with higher levels of concentration, and in systems characterized by high rates of deposition.

This model provides reasonable trends with respect to the coating evolution on nanoscale structures and how that evolution depends on process parameters. To become more useful to the application engineer, we must now benchmark the model against experimental data as processing parameters are varied. However, it is difficult to quantitatively compare the results from the polar geometry model since most TEM data is relevant to the longitudinal configuration of the nanofiber and not the cross-sectional configuration.

Hence, the intent of the present article is to replicate the local transport and deposition analysis of Part II[2] posed in an axisymmetric coordinate system. The concentration field is still radially dominant, but we use the complete expression without replacing the location of the coating surface with the radius of the uncoated nanofiber. Further, we remove the single-valued assumption to examine more complex coating surface structures. With a model validated against experimental data we can then predict how coating properties will change with deposition conditions for similar geometries. This predictive capability will be quite useful as the size of solid-state optoelectronic components continues to decrease.

For the remainder of this article, we only consider the nanofiber region and transport of the deposition material by diffusion. Mass balance equations at the coating surface include deposition rate parameters and desorption parameters due to ion bombardment. These parameters are functions of the fiber and coating curvature, the ion flux to the coating surface, and the ion kinetic energy. These parameters are passed to the continuum equations from the molecular dynamics (MD) simulations in Part II.[2]

At the local nanofiber scale, the evolution equation for the coating free surface contains four basic components of the coating mechanism. These are attachment kinetics, curvature effects, etching due to ion bombardment, and solid-state diffusion on the coating surface. This equation is solved numerically and analyzed via boundary perturbation techniques. The initial polymer nanofiber landscape is taken to be a superposition of Fourier modes, consistent with models of the electrospinning process.[4,5] Hence, our approach links models across the entire fabrication process. Results from these analyses are shown to verify basic experimental observations; for example, the wavelength and magnitude of the coating roughness is larger in the axial direction for larger diameter fibers.

III. NEUTRAL SPECIES TRANSPORT MODEL

A. Fomulation

The objective of the model is to determine the influence of process conditions on the uniformity and morphology of the coating. The system is characterized by a bulk gas phase dominated by neutral species and sheath regions that separate the bulk gas phase from the substrate (nanofibers) and the target, as shown in Fig. 1. There are several disparate geometrical length scales in the reactor system. The reactor size from the target to the top is no more than 20 cm in length. The distance from the target to the holder is centimeters in length. Sheath regions are several millimeters in thickness, while nanofibers range from 20 to 100 nm in diameter. In our modeling effort, we treat each nanofiber within the mat as an isolated fiber, and also assume that the holder region of nanofibers does not influence the global transport of neutral species. As noted above, however, a sheath region that influences ion transport does exist in the region of the holder and its mat of nanofibers.

The transport of neutral species is separated into two components: (1) a one-dimensional reactor-scale model and (2) a two-dimensional local nanofiber-scale model. The reactor-scale model, the focus of Ref. 1, includes the sheath region near the target and transport throughout the reactor, but ignores the presence of the holder region. The present article focuses on the transport of neutral species in the vicinity of a typical nanofiber. With these assumptions, the two articles are linked as follows: The reactor-scale model provides the far-field (half the distance away from an adjacent fiber) input of the neutral species concentration, C^*, at location $\hat{y}=y^*$ of a particular nanofiber as shown in Fig. 1. Figure 3 provides a schematic of the region near a nanofiber. The cylindrical fiber is encapsulated by a nonuniform coating of neutral species. Outside of the coating we suppose a sheath region exists and that the far field neutral species concentration is C^*. We note that the reactor-scale model[1] predicts that this concentration is constant throughout the reactor, except, of course, in the vicinity of the fiber, which is the topic of the present article.

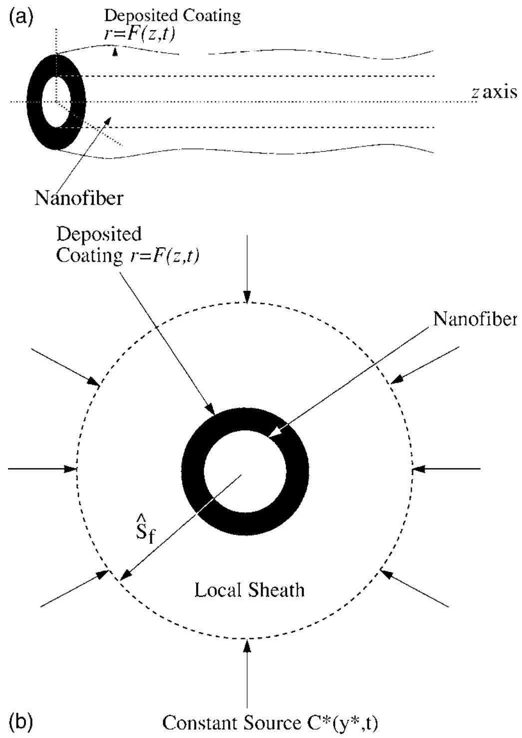

FIG. 3. Local model for neutral species transport near the nanofiber (not drawn to scale or proportion). (a) Side view. (b) End view.

In Ref. 1 the dimensional concentration C^* of the neutral species at the reactor scale was found to be the constant

$$C^* = \frac{k_{\mathrm{ions}}}{k}, \tag{1}$$

where k is a reaction coefficient for sputtered material readsorbing to the target surface and k_{ions} is the desorption rate coefficient for sputtering due to ion bombardment of the target surface. These rate coefficients depend on the ion flux to the surface and the ion kinetic energy. These two quantities were obtained by examining the sheath region around the target. Once determined, these quantities were passed to the MD simulations to determine k and k_{ions}. Knowing these parameters, the concentration C^* was then determined in the reactor as a function of the reactor operating conditions. This concentration field serves as the input for the local transport model as shown in Fig. 3. Given the sparseness of the nanofiber mesh, it is assumed that the concentration C^* away from a nanofiber is unaffected by any loss of depositing species due to deposition. However, the concentration near the nanofiber does change due to the deposition. Note also that the units of concentration are mole/volume, the units of k are length/time, and the units of k_{ions} are mole/(area × time).

For the local nanofiber scale transport model around a single nanofiber, consider a cylindrical geometry as shown in Fig. 3. This particular nanofiber is located at a distance $\hat{y} = y^*$ from the target as shown in Fig. 1. The goal is to determine the location, $\hat{r} = \hat{F}(\hat{z}, \hat{t})$, of the front of the deposited coating. Table I lists the variables used in the model and Table II lists ranges of values for the parameters used in the model. The controllable operating conditions for the reactor are pressure, power, temperature, target-nanofiber distance, mat porosity, and initial nanofiber radius. These parameters and ranges of their values were discussed in Refs. 1 and 2 of this article. From these representative values we extracted the information listed in Table II and used in the results that follow.

Assume the source of the deposition material is given by C^*, and is located at $\hat{r} = \hat{S}_F$, where $\hat{S}_F$ is half the average spacing between fibers in the mat. This value C^* remains constant around the nanofiber because the fiber is so small in comparison to the global reactor scale. Since C^* is a result of the sputtering process and depends on the reactor operating conditions, we have linked the *local and global* models through the condition at $\hat{r} = \hat{S}_F$.

Within the local region surrounding a fiber $\{\hat{F}(\hat{z}, \hat{t}) \leq \hat{r} \leq \hat{S}_F\}$, assume that the concentration $\hat{c}$ of deposition material (neutral gas molecules) is large compared to the ion concentration, and that the mode of transport of the deposition material is primarily governed by diffusion

$$\hat{c}_{\hat{t}} = \hat{D}\left[\hat{c}_{\hat{r}\hat{r}} + \frac{1}{\hat{r}}\hat{c}_{\hat{r}} + \frac{1}{\hat{r}^2}\hat{c}_{\hat{z}\hat{z}}\right], \tag{2}$$

where $\hat{D}$ is the diffusivity.

At the coating front $\{\hat{r} = \hat{F}(\hat{z}, \hat{t})\}$, the diffusive flux of neutral species equals the net rate of deposition due to Eq. (1) deposition (or reaction) from the bulk phase and Eq. (2) desorption due to ion bombardment of the coating surface. These two processes correspond to the respective terms on the right-hand side of

$$\hat{D}\,\nabla\,\hat{c}\cdot\hat{n} = k_F(\hat{z}, \hat{I}_F^+, \hat{\varepsilon}_F^+, \hat{t})\hat{c}[1 + \hat{\Gamma}\hat{\kappa}] - k_{\mathrm{Fions}}(\hat{z}, \hat{I}_F^+, \hat{\varepsilon}_F^+, \hat{t}). \tag{3}$$

Equations of this form have been previously proposed in Refs. 6–8. Here k_F is a reaction coefficient, $\hat{\Gamma}$ the capillary length scale, $\hat{\kappa}$ the curvature of the front, k_{Fions} the desorption rate coefficient due to ion bombardment of the coating surface, $\hat{I}_F^+$ the ion flux to the surface, and $\hat{\varepsilon}_F^+$ the ion kinetic energy. The reaction and desorption coefficients k_F and k_{Fions} are obtained using MD simulations of attachment to and detachment from a uniform cylindrical nanofiber coating. This analysis is described in Part II.[2]

The normal velocity of the coating front $\hat{v}_n$ is needed to simulate the film growth at this length scale. The normal front velocity is taken to be

$$\hat{v}_n = k_F\beta\hat{c}[1 + \hat{\Gamma}\hat{\kappa}] - \beta k_{\mathrm{Fions}} - \psi_s D_s \hat{\Gamma}\frac{\partial^2\hat{\kappa}}{\partial\hat{s}^2}, \tag{4}$$

where β is the molar volume, $\hat{s}$ the arclength along the coating front, and ψ_s the thickness of the coating film that participates in the surface diffusion phenomenon. The units for β are determined by $\beta = (\mathrm{mwt})(1/\mathrm{density}) = \mathrm{vol}/\mathrm{mole}$, where the density is that for the coating in the solid phase and mwt is the molecular weight of the coating material. Equations similar to Eq. (4) have been proposed by Refs. 8 and 9 for chemical vapor deposition onto flat substrates.

All of the terms in Eq. (4) are evaluated on the front, $\hat{r} = \hat{F}(\hat{z}, \hat{t})$. The first two terms in this equation are the contri-

TABLE I. Glossary.

Term	Description	Units
$\hat{z}$	Dimensional location on the axial axis	nm
$\hat{t}$	Dimensional time	s
$\hat{c}$	Dimensional concentration of the deposition material	mole/nm^3
$\hat{r}=\hat{F}(\hat{z},\hat{t})$	Dimensional location of the coating front	nm
z	Nondimensional location on the axial axis	
t	Nondimensional time	
c	Nondimensional concentration of the deposition material	
$r=F(z,t)$	Nondimensional location of the coating front	
C^*	Dimensional concentration of the neutral species	mole/nm^3
k_{ions}	Desorption rate coefficient for sputtering at the target	mole/nm^{2}s
k	Reaction coefficient for sputtered material at the target	nm/s
$\hat{y}=y^*$	Distance from target to the nanofiber	nm
$\hat{S}_F$	Half of the average spacing between the fibers in the mat	nm
$\hat{D}$	Diffusivity	nm^2/s
k_F	Reaction coefficient at the fiber	nm/s
$\hat{\Gamma}$	Capillary length scale	nm
$\hat{\kappa}$	Curvature of the coating front	1/nm
$\hat{R}_F$	Original fiber radius	nm
k_{Fions}	Desorption rate due to ion bombardment	mole/nm^{2}s
Γ_F^+	Ion flux to the surface	mole/nm^{2}s
$\hat{\varepsilon}_F^+$	Ion kinetic energy	eV
$\hat{v}_n$	Normal velocity of the coating front	nm/s
β	Molar volume	nm^3/mole
$\hat{s}$	Arc length along the coating front	nm
ψ_s	Thickness of the coating film that participates in the surface diffusion	nm
D_s	Diffusivity of the atoms on the coating front	nm^2/s
$\hat{n}$	Normal vector to the coating front	
$\hat{f}(\hat{t})$	Base state growth front	nm
$\hat{L}_F$	Length of the nanofiber	nm
$\hat{K}$	Wave number	1/nm
λ	Wavelength of the coating	nm
D_{k_F}	Damköhler number	
Q_F	Ratio of the rate of front motion to the rate of diffusion	
v_n	Nondimensional normal velocity of the coating front	
ε_F	Fiber aspect ratio	
κ	Nondimensional curvature	
R_F	Nondimensional radius	
$\delta H(z,t)$	Nondimensional location of the surface of a thin coating	
K	Nondimensional wave number	
K_{critical}	Wave number at which coating growth is most unstable	
ρ	Parameter used for arc-length interface representation	

butions to the normal velocity due to deposition and desorption, and the third term is diffusion along the coating surface. Here D_s is the diffusivity of the adatoms on the coating surface.

The curvature of the front is defined by

$$\hat{\kappa}(\hat{z}) = \frac{-1}{\hat{F}\sqrt{1+\hat{F}_{\hat{z}}^2}} + \frac{\hat{F}_{\hat{z}\hat{z}}}{[1+\hat{F}_{\hat{z}}^2]^{3/2}}. \qquad (5)$$

The normal vector to the coating front is

TABLE II. Approximate values of parameters from Refs. 1 and 2.

Parameter	Approximate value
$\hat{S}_F$	75 to 500 nm
k_{Fions}	5.58×10^{-26} mole/nm^{2}s
k_F	3×10^{11} to 3×10^{13} nm/s
C^*	3×10^{-37} to 3×10^{-36} mole/nm^3
$\hat{D}$	7.5×10^{13} nm^2/s
β	9.6×10^{21} nm^3/mole
$\hat{\Gamma}$	0.0505 nm
$\psi_s D_s$	6.5×10^{3} nm^3/s
$\hat{R}_F$	13 to 73 nm
$\hat{L}_F$	500 to 4000 nm

$$\hat{n} = \frac{\langle 1, -\hat{F}_{\hat{z}} \rangle}{\sqrt{1 + \hat{F}_{\hat{z}}^2}}. \tag{6}$$

The normal front velocity $\hat{v}_n$ in cylindrical coordinates is given by

$$\hat{v}_n = \frac{\hat{F}_{\hat{t}}}{\sqrt{1 + \hat{F}_{\hat{z}}^2}}. \tag{7}$$

Setting Eq. (4) equal to Eq. (7), we develop the evolution equation

$$k_F \beta \hat{c}[1 + \hat{\Gamma}\hat{\kappa}] - \beta k_{\text{Fions}} - \psi_s D_s \hat{\Gamma} \frac{\partial^2 \hat{\kappa}}{\partial \hat{s}^2} = \frac{\hat{F}_{\hat{t}}}{\sqrt{1 + \hat{F}_{\hat{z}}^2}}, \tag{8}$$

that describes the shape of the coating front. Note that for large $\hat{F}$, Eq. (8) reduces to the model for deposition onto a flat substrate presented in Ref. 8.

The governing equations and boundary conditions are nondimensionalized using the following scalings:

Dimensional variable	Scale
$\hat{z}$	$\hat{L}_F$
$\hat{c}$	C^*
$\hat{r}$	$\hat{S}_F$
$\hat{t}$	$\hat{S}_F/(k_F \beta C^*)$
$\hat{s}$	$\hat{S}_F$
$\hat{F}$	$\hat{S}_F$
$\hat{\kappa}$	$1/\hat{S}_F$

where $\hat{L}_F$ is the length of the nanofiber. Dimensionless variables are hatless.

These scalings lead to the nondimensional groups:

$$D_{k_F} = (k_F \hat{S}_F)/\hat{D},$$

$$\Gamma = \hat{\Gamma}/\hat{S}_F,$$

$$Q_F = \frac{k_F \hat{S}_F \beta C^*}{\hat{D}},$$

$$\varepsilon_F = \frac{\hat{S}_F}{\hat{L}_F},$$

where D_{k_F}, the Damköhler number, is the ratio of the rate of deposition on the fiber to the rate of neutral species transport by diffusion, Q_F is the ratio of the rate of front motion to the rate of diffusion of the neutral species, and ε_F is the fiber aspect ratio.

The nondimensional governing equation for concentration is

$$Q_F c_t = c_{rr} + \frac{1}{r} c_r + \varepsilon_F^2 c_{zz}, \quad \text{for} \quad F(z,\, t) < r < 1. \tag{9}$$

Here, $F(z,\, t) = \hat{F}(\hat{z},\, \hat{t})/\hat{S}_F$ is the dimensionless coating thickness.

We impose two spatial boundary conditions upon the concentration field. At the edge of the local region $(r=1)$, the concentration is uniform as predicted by the reactor scale model

$$c = 1. \tag{10}$$

At the edge of the coating $[r=F(z,t)]$ we apply the dimensionless version of Eq. (3)

$$\frac{c_r - \varepsilon_F^2 F_z c_z}{\sqrt{1 + (\varepsilon_F F_z)^2}} = D_{k_F} c[1 + \Gamma\kappa] - \frac{k_{\text{Fions}} \hat{S}_F}{C^* \hat{D}}, \tag{11}$$

where

$$\kappa = \frac{-1}{F\sqrt{1 + (\varepsilon_F F_z)^2}} + \frac{\varepsilon_F^2 F_{zz}}{[1 + (\varepsilon_F F_z)^2]^{3/2}} \tag{12}$$

is the nondimensional curvature from Eq. (5).

Setting Eq. (4) equal to Eq. (7), we find the evolution equation for the coating front to be

$$\frac{F_t}{\sqrt{1 + (\varepsilon_F F_z)^2}} = c[1 + \Gamma\kappa] - \frac{k_{\text{Fions}}}{k_F C^*} - \frac{\psi_s D_s}{\beta C^* k_F \hat{S}_F^2} \Gamma \frac{\partial^2 \kappa}{\partial s^2}. \tag{13}$$

Here, $\partial^2\kappa / \partial s^2 = \varepsilon_F^2 [\kappa_z / \sqrt{1 + (\varepsilon_F^* F_z)^2}]_z \big/ \sqrt{1 + (\varepsilon_F F_z)^2}$ is the second derivative of the curvature with respect to arc length. Therefore, the evolution Eq. (13) becomes

$$\frac{F_t}{\sqrt{1 + (\varepsilon_F F_z)^2}} = c[1 + \Gamma\kappa] - \frac{k_{\text{Fions}}}{k_F C^*} - \frac{\psi_s D_s \Gamma}{\beta C^* k_F \hat{S}_F^2} \frac{\varepsilon_F^2 [\kappa_z / \sqrt{1 + (\varepsilon_F F_z)^2}]_z}{\sqrt{1 + (\varepsilon_F F_z)^2}}. \tag{14}$$

This expression is used to determine the dynamic location of the coating front.

B. Solution by boundary perturbation

Three assumptions are required to make analytical progress in the solution of the Eqs. (9), (11), and (14): (1) the rate of growth of the front compared to the rate of diffusional transport is negligible ($Q_F \ll 1$ so the system is quasistatic); (2) the coating is nearly circular; and (3) derivatives of the concentration and of the two rate constants with respect to z are negligible at leading order.

The second assumption above corresponds to the perturbation expansion

$$F(z,t) = f(t) + Ag(z,\, t), \; A \ll 1, \tag{15}$$

where $A = \hat{A}/S_F$, and g is a small perturbation (with amplitude $\hat{A}$) of the boundary front from the growing circular front $r=f(t)$. The third assumption is equivalent to the concentration field c possessing the following perturbation expansion:

$$c = c_0(r,t) + Ac_1(r,z,t) + \cdots. \tag{16}$$

In the above, the leading order term is independent of z, but may depend upon $f(t)$.

The details of the asymptotic solution procedure of the boundary perturbation method are identical to the Appendix of Part II.[2] As expected, the leading order results for the location of the circular coating shape are also identical and are not repeated here. We note that the numerical simulations of the evolution equation that follow reproduce the boundary perturbation results when a flat-shape initial condition is posed.

IV. WEAKLY NONLINEAR SOLUTION

A. Formulation and solution

As above we assume the concentration field is quasisteady $Q_F \ll 1$ and that the shape of the coating front does not significantly influence the transport of c in the z direction. For the weakly nonlinear solution, we take $r=F(z,\ t)$ and pose

$$c = c_0(r,\ z,\ t) + \varepsilon_F c_1(r,\ z,\ t) + \cdots,\ \varepsilon_F \ll 1. \tag{17}$$

This is similar to the solution forms used in the boundary perturbation analysis, except that the front shape is no longer expanded. Notice that these assumptions result in a simplified version of Eq. (2). However, the full form of Eq. (8) is still used. In essence, we allow large derivatives with respect to z in Eq. (8) but only include small derivatives in z for the concentration. This allows us to derive a simple analytical solution to Eq. (2) rather than perform a numerical simulation of this equation.

By straightforward asymptotic analysis we find the concentration to be

$$c = 1 + \left[\frac{D_{k_F}(F-\Gamma) - \frac{k_{\text{Fions}}\hat{S}_F F}{C^* \hat{D}}}{1 - D_{k_F} \ln(F)(F-\Gamma)} \right] \ln r + O(\varepsilon_F^2). \tag{18}$$

Substituting this solution into Eq. (14) we find the evolution equation to be

$$\frac{F_t}{\sqrt{1+(\varepsilon_F F_z)^2}} = \left[1 + \frac{D_{k_F}(F-\Gamma) - \frac{k_{\text{Fions}}\hat{S}_F F}{C^* \hat{D}}}{1 - D_{k_F} \ln(F)(F-\Gamma)} \right] \ln F[1 + \Gamma\kappa] - \frac{k_{\text{Fions}}}{k_F C^*} - \frac{\psi_s D_s}{\beta C^* k_F \hat{S}_F^2} \Gamma \frac{\partial^2 \kappa}{\partial s^2}, \tag{19}$$

which describes the moving front of the coating. This evolution equation is subject to periodic boundary conditions in z and along its length

$$F(0) = F(1),\ F'(0) = F'(1),\ F''(0) = F''(1), \quad \text{and} \quad F'''(0) = F'''(1). \tag{20}$$

Numerical solutions of Eq. (19) are investigated in Sec. V B.

B. Linearization of the evolution equation

The moving front of the coating $r=F(z,t)$ is defined as the solution to Eq. (19), where

$$\kappa = \frac{-1}{F\sqrt{1+(\varepsilon_F F_z)^2}} + \frac{\varepsilon_F^2 F_{zz}}{[1+(\varepsilon_F F_z)^2]^{3/2}}.$$

To linearize this equation for analytical discussion we assume that $r=F(z,\ t)$ takes the form

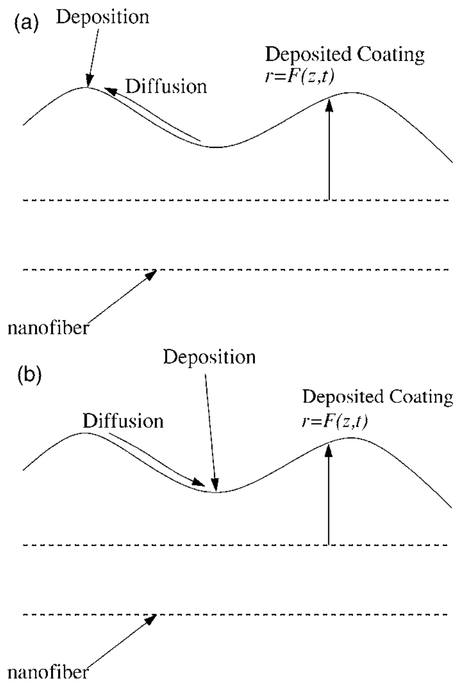

FIG. 4. The effect of destabilizing and stabilizing terms (not drawn to scale or proportion). (a) Destabilizing. (b). Stabilizing.

$$r = F(z,\ t) = R_F + \delta H(z,\ t), \tag{21}$$

where R_F is the nondimensional radius of the uncoated fiber and $\delta \ll 1$. Physically, this describes F as the initial fiber radius R_F with a thin coating described by $H(z,\ t)$. This thin coating has a thickness of order δ. It must be noted that this study of thin coating thickness is only valid for early times. With this in mind we also assume that $D_{k_F} = D^* \delta$ in order to study slow coating growth. Here D^* is an $O(1)$ constant.

The leading order problem from Eq. (19) is

$$0 = \left[1 - \frac{\Gamma}{R_F} \right] - \frac{k_{\text{Fions}}}{k_F C^*}. \tag{22}$$

This condition is also required for a thin coating. Qualitatively, this condition occurs when the rate of deposition balances the rate of etching.

Under these assumptions we linearize the evolution equation to find

$$H_t = \Gamma\left(\varepsilon_F^2 H_{zz} + \frac{H}{R_F^2} \right) - \frac{\psi_s D_s}{\beta C^* k_F \hat{S}_F^2} \Gamma \varepsilon_F^2 \left(\frac{H_{zz}}{R_F^2} + \varepsilon_F^2 H_{zzzz} \right). \tag{23}$$

In Eq. (23), there is a competition between terms contributing to the growth rate H_t. In general, all of the competing terms relate to energy. The coating seeks the lowest energy state that minimizes curvature. In a radial sense, this means a larger radius, while in the axial sense, this means a more uniform coating along the length of the fiber. Thus, in Fig. 4, we define destabilizing terms as those that cause diffusion and deposition to the peaks while stabilizing terms as those that cause diffusion and deposition to valleys.

Analyzing Eq. (23), we see that the first grouping of terms to the right of the equality are related to the curvature

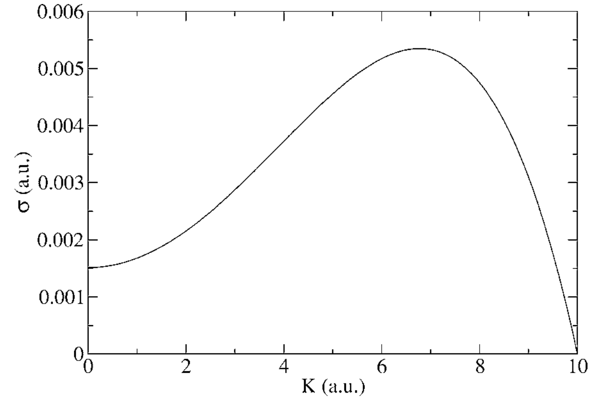

FIG. 5. Nondimensional plot of σ ($\psi_s D_s = 6.5\times10^3\frac{\text{nm}^3}{\text{s}}$, $k_F = 7.5\times10^{12}\frac{\text{nm}}{\text{s}}$, $C^* = 3\times10^{-36}\frac{\text{mole}}{\text{nm}^3}$, $\hat{S}_F = 75$ nm, $\hat{R}_F = 50$ nm, $\hat{L}_F = 500$ nm, $\beta = 9.6\times10^{21}\frac{\text{nm}^3}{\text{mole}}$).

(lengthwise and radially) of the coating surface. Thus, H_{zz} can be described as a stabilizing term along the length of the fiber. The curvature is positive in the valleys and thus this term results in deposition in the valleys. Contrary to this, the term H/R_F^2 has a destabilizing effect. Therefore, this term causes more to be deposited at the peaks (where there is a larger H value). This latter description is relative to the initial radius. Hence, less effect is seen at larger initial radii.

The second group of terms $-(H_{zz}/R_F^2) - \varepsilon_F^2 H_{zzzz}$ describes the effects of surface diffusion. At the peaks of the coating $-H_{zz}$ is positive, which leads to a destabilizing effect. Therefore, this term relates to diffusion from valleys to peaks in order to make the radius larger and achieve a flatter radial coating. On the other hand, $-\varepsilon_F^2 H_{zzzz}$ provides a stabilizing effect and thus it describes the diffusion from peaks to valleys. Physically, the first term attempts to cause a smoother surface in the radial direction while the second term attempts to create a uniform coating along the fiber axis.

C. Solution of the linearized evolution equation

We seek solutions to Eq. (23) of the form $H(z,t) = Ae^{\sigma t}e^{iKz}$. This solution represents a periodic coating in the axial direction. Here, K represents the nondimensional wave number. The wavelength in the axial direction is $\lambda = 2\pi/\hat{K}$, where $\hat{K} = K/\hat{L}_F$. The amplitude of this periodic coating surface is controlled by the $Ae^{\sigma t}$ term. Thus, if the growth rate $\sigma > 0$, a nonuniform and unstable coating is formed.

Substituting $H(z,t) = Ae^{\sigma t}e^{iKz}$ into Eq. (23), we obtain an expression for the growth rate

$$\sigma = -\frac{\psi_s D_s \varepsilon_F^4 \Gamma}{\beta C^* k_F \hat{S}_F^2}K^4 + \frac{\psi_s D_s \varepsilon_F^2 \Gamma}{\beta C^* k_F \hat{S}_F^2 R_F^2}K^2 - \varepsilon_F^2 \Gamma K^2 + \frac{\Gamma}{R_F^2}. \quad (24)$$

Here, the first two terms are linked to the surface diffusion terms in Eq. (23) while the last two terms are linked to the deposition terms in the same equation. The terms that are negative are stabilizing terms while the terms that are positive are destabilizing terms. Using data from Table II, we plot Eq. (24) in Fig. 5. It is seen that long waves are unstable. The peak represents the value for K at which the growth is most unstable.

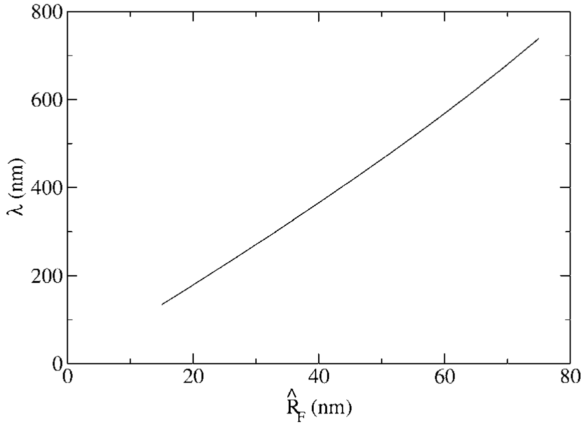

FIG. 6. Dimensional plot of the critical value of λ as a function of $\hat{R}_F$ ($\psi_s D_s = 6.5\times10^3\frac{\text{nm}^3}{\text{s}}$, $k_F = 7.5\times10^{12}\frac{\text{nm}}{\text{s}}$, $C^* = 3\times10^{-36}\frac{\text{mole}}{\text{nm}^3}$, $\hat{S}_F = 75$ nm, $\hat{L}_F = 500$ nm, $\beta = 9.6\times10^{21}\frac{\text{nm}^3}{\text{mole}}$).

When $\psi_s D_s \varepsilon_F^2 \Gamma / \beta C^* k_F \hat{S}_F^2 R_F^2 < \varepsilon_F^2 \Gamma$, or $\psi_s D_s / \beta C^* k_F \hat{S}_F^2 R_F^2 < 1$, the peak occurs at $K = 0$, otherwise the peak occurs at

$$K_{\text{critical}} = \sqrt{\frac{\dfrac{\psi_s D_s}{\beta C^* k_F \hat{S}_F^2 R_F^2} - 1}{2\dfrac{\psi_s D_s \varepsilon_F^2}{\beta C^* k_F \hat{S}_F^2}}}. \quad (25)$$

In the former case that $\psi_s D_s \varepsilon_F^2 \Gamma / \beta C^* k_F \hat{S}_F^2 R_F^2 < \varepsilon_F^2 \Gamma$ dominates, the coating grows radially with no bumps. In other words, the wavelength is so large that the coating appears to be uniform in the axial direction. Physically, this occurs because the dominating term in the expression (24) for the growth rate relates to uniform deposition along the fiber, thus forming a growing but uniform coating.

Equation (25) can be rewritten as

$$K_{\text{critical}} = \hat{L}_F \sqrt{\frac{\dfrac{\psi_s D_s}{\beta C^* k_F \hat{S}_F^2 \hat{R}_F^2} - 1}{2\dfrac{\psi_s D_s}{\beta C^* k_F}}}. \quad (26)$$

Dividing by the fiber length, we have

$$\hat{K} = \sqrt{\frac{\dfrac{\psi_s D_s}{\beta C^* k_F \hat{S}_F^2 \hat{R}_F^2} - 1}{2\dfrac{\psi_s D_s}{\beta C^* k_F}}}. \quad (27)$$

Thus, the critical wavelength is independent of the fiber length. By using the input data from Fig. 5, we are able to estimate the size of K_{critical}. We find that the nondimensional K_{critical} is estimated to be 6.7710, as can be seen in Fig. 5. Using $\lambda = 2\pi/\hat{K}$, we find the corresponding wavelength to be 463.98 nm. This wavelength is less than the results seen in Ref. 8 for deposition onto a flat substrate. This is due to the different material parameters used in their model. One should note that this model neglects any instabilities in the θ direction. These instabilities were the topic of Part II.[2]

Analyzing the equation for K_{critical}, we see that as $\hat{R}_F$ increases, K_{critical} decreases, which results in an increase of the critical wavelength λ. These results are shown in Fig. 6, with $\hat{R}_F$ varied between 15 and 75 nm.

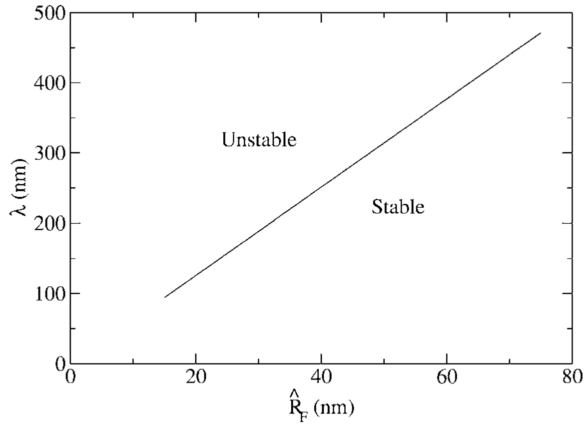

FIG. 7. Neutral stability curve for λ as a function of $\hat{R}_F$ ($\psi_s D_s = 6.5 \times 10^3 \frac{\text{nm}^3}{\text{s}}$, $k_F = 7.5 \times 10^{12} \frac{\text{nm}}{\text{s}}$, $C^* = 3 \times 10^{-36} \frac{\text{mole}}{\text{nm}^3}$, $\hat{S}_F = 75$ nm, $\hat{L}_F = 500$ nm, $\beta = 9.6 \times 10^{21} \frac{\text{nm}^3}{\text{mole}}$).

We determine the values of K for which $\sigma \leq 0$, to determine the neutral stability curve. We find that $\sigma \leq 0$ when the inequality

$$K > \sqrt{\frac{-\left(\frac{\psi_s D_s \Gamma}{\beta C^* k_F \hat{S}_F^2 R_F^2} - \Gamma\right) - \sqrt{\left(\frac{\psi_s D_s \Gamma}{\beta C^* k_F \hat{S}_F^2 R_F^2} - \Gamma\right)^2 + 4\left(\frac{\psi_s D_s \Gamma}{\beta C^* k_F \hat{S}_F^2}\right)\left(\frac{\Gamma}{R_F^2}\right)}}{-2\frac{\psi_s D_s \varepsilon_F^2 \Gamma}{\beta C^* k_F \hat{S}_F^2}}}, \tag{28}$$

holds. This relation is plotted in Fig. 7. Notice that as $\hat{R}_F$ increases, the maximum wavelength for a stable solution increases. Hence, one should observe longer wavelength patterns developing experimentally in the axial direction on larger diameter fibers. This is qualitatively consistent with the results shown in Figs. 2(b) and 2(c). Furthermore, it appears that the predicted magnitudes of the wavelengths are comparable to those observed in these same figures.

V. NUMERICAL SIMULATIONS OF THE COATING SURFACE

A. Parametrization

The speed of the moving front of the coating at $r = F(z, t)$ is defined by

$$\begin{aligned} v_n &= \frac{F_t}{\sqrt{1 + (\varepsilon_F F_z)^2}} \\ &= \left[1 + \frac{D_{k_F}(F - \Gamma) - \frac{k_{\text{Fions}} \hat{S}_F F}{C^* \hat{D}}}{1 - D_{k_F} \ln(F)(F - \Gamma)}\right] \ln F[1 + \Gamma\kappa] - \frac{k_{\text{Fions}}}{k_F C^*} \\ &\quad - \frac{\psi_s D_s}{\beta C^* k_F \hat{S}_F^2} \Gamma \frac{\partial^2 \kappa}{\partial s^2}, \end{aligned} \tag{29}$$

which also defines the evolution equation for the front. We seek solutions to this equation subject to periodic conditions along the fiber length

$$F(0) = F(1), \; F'(0) = F'(1), \; F''(0) = F''(1), \quad \text{and} \quad F'''(0) = F'''(1).$$

A single-valued representation of the coating interface cannot be used to simulate coatings that are multivalued in the z coordinate such as that shown in Fig. 2(a). Thus, we use an arc-length strategy.[8,10–12] This strategy parametrizes the cylindrical coordinates z and F using the normalized arc length of the coating front. Here, the normalized arc-length ρ becomes the independent variable, while both F and z are dependent variables of ρ. Hence, a multivalued function in the z coordinate becomes a single-valued function in ρ. Since the horizontal and vertical coordinates are now functions of ρ, the notation $z = z(\rho)$ and $F = F(\rho)$ will be used.

In this strategy the dimensional arc-length $\hat{s}$ is defined as

$$\hat{s}(\rho) = \int_0^{\rho} \sqrt{\hat{z}_{\wp}^2 + \hat{F}_{\wp}^2}\, d\wp, \tag{30}$$

which results in the nondimensional derivative expression

$$\frac{\partial}{\partial s} = \frac{\varepsilon_F}{\sqrt{z_\rho^2 + (\varepsilon_F F_\rho)^2}} \frac{\partial}{\partial \rho}. \tag{31}$$

With $\partial / \partial s$ found, the curvature κ can be parametrized. The parametrized nondimensional curvature is

$$\kappa(\rho) = \frac{-|z_\rho|}{F\sqrt{z_\rho^2 + (\varepsilon_F F_\rho)^2}} + \frac{\varepsilon_F^2 (F_{\rho\rho} z_\rho - z_{\rho\rho} F_\rho)}{[z_\rho^2 + (\varepsilon_F F_\rho)^2]^{3/2}}. \tag{32}$$

The parametrized unit normal vector to the coating surface is

$$\hat{n} = \frac{(-\hat{F}_\rho, \hat{z}_\rho)}{\sqrt{\hat{z}_\rho^2 + \hat{F}_\rho^2}} = \frac{(-\varepsilon_F F_\rho, z_\rho)}{\sqrt{z_\rho^2 + (\varepsilon_F F_\rho)^2}}. \tag{33}$$

With the unit normal vector defined, the velocity of the coating front can be expressed as

$$\vec{v} = \left(\frac{\partial \hat{z}}{\partial \hat{t}}, \frac{\partial \hat{F}}{\partial \hat{t}}\right) = \hat{v}_n \hat{n}, \tag{34}$$

where $\hat{v}_n$ is the dimensional form of the coating speed in Eq. (29). Equation (34) can be separated into the pair of nondimensional differential equations

$$\frac{\partial z}{\partial t} = \frac{-\varepsilon_F^2 F_\rho}{\sqrt{z_\rho^2 + (\varepsilon_F F_\rho)^2}} v_n, \tag{35}$$

$$\frac{\partial F}{\partial t} = \frac{z_\rho}{\sqrt{z_\rho^2 + (\varepsilon_F F_\rho)^2}} v_n, \tag{36}$$

where v_n is written in terms of the parameter ρ.

B. Numerical results

For specified parameter sets and initial interface locations, Eqs. (35) and (36) are solved numerically to determine the evolution of the coating interface. Here the initial location of the interface is considered to be coating material already on the fiber rather than the bare fiber itself. Also note that unless stated otherwise, parameter values from Table II are used in the numerical simulations.

Equations (35) and (36) are solved simultaneously. In the numerical solution procedure, the chosen initial interface is discretized using a uniform grid. A predetermined number of points are chosen and the spatial derivatives at each point are

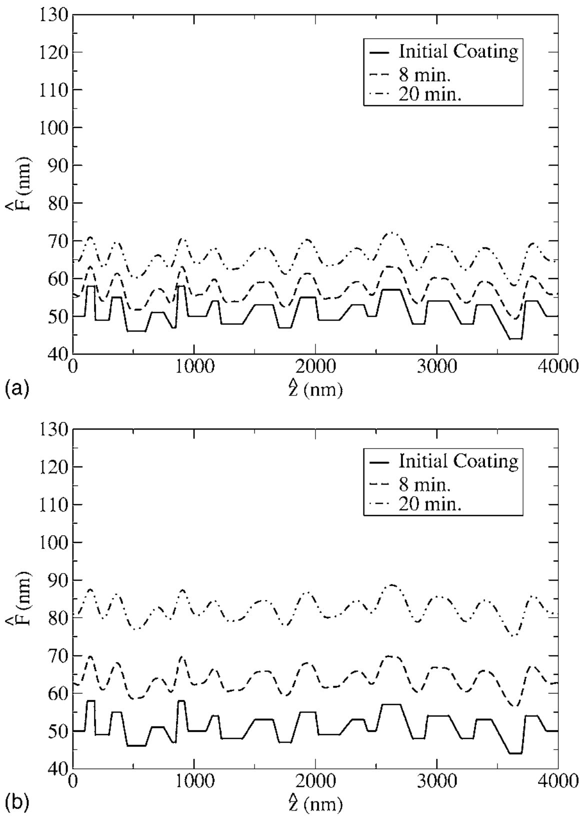

FIG. 8. Dimensional axial plot of the coated fiber ($C^*=3\times10^{-36}\frac{\text{mole}}{\text{nm}^3}$, $\hat{L}_F=4000$ nm, $\hat{S}_F=200$ nm). (a) $k_F=7.5\times10^{11}\frac{\text{nm}}{\text{s}}$. (b) $k_F=7.5\times10^{12}\frac{\text{nm}}{\text{s}}$.

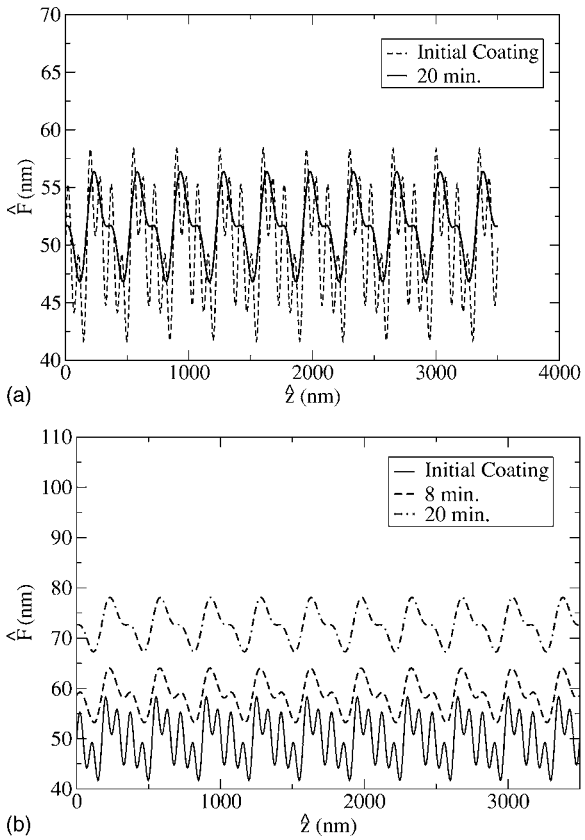

FIG. 9. Dimensional axial plot of the coated fiber ($k_F=7.5\times10^{11}\frac{\text{nm}}{\text{s}}$, $\hat{L}_F=4000$ nm, $\hat{S}_F=75$ nm). (a) $C^*=3\times10^{-37}\frac{\text{mole}}{\text{nm}^3}$. (b) $C^*=3\times10^{-36}\frac{\text{mole}}{\text{nm}^3}$.

approximated using finite difference formulas. The differential equations are solved using the optimal third-order TVD Runge-Kutta scheme. This scheme is chosen because it is designed to diminish oscillations due to instabilities in the numerical scheme. A description and formulation of this method can be found in Ref. 13. Due to the nature of the time scalings, the stability of the code depends on parameter values. Also, because of curvature and curvature derivative terms, the stability of the code is dependent on the coating morphology. In general, the relation between the maximum allowable time step Δt and grid spacing $\Delta\rho$ follows $\Delta t \propto (\Delta\rho)^4$. Computing time is generally around 12 h on a Pentium 4 3.4 GHz machine. To validate the stability of the numerical solution procedure, solutions were calculated using the time steps Δt, $\Delta t/2$, and $\Delta t/10$ for a fixed grid spacing. Additionally, the grid spacings were varied from $\Delta\rho$ to $\Delta\rho/5$. In all cases there were no noticeable variations seen in the solutions.

Results for an increasing reaction coefficient k_F are shown in Fig. 8. Increasing k_F results in increasing the Damköhler number D_{k_F}. Results show that an increase in D_{k_F} results in an increase in coating deposition, as expected. Notice that as the coating grows, the sharp corners of the initial coating profile become smoother. Here, diffusion smooths out any roughness in the coating. Also notice that the coating, for the most part, maintains its initial peaks and valleys at this time frame, with neither growing significantly faster than the other.

Results for initial conditions composed of a superposition of sine functions and for varying concentration are presented in Figs. 9 and 10. As expected, a larger concentration source C^* causes an increase in coating growth. In Fig. 9, it is important to notice that as the coating grows, some of the peaks and valleys are smoothed out and no longer appear in the coating morphology. This is consistent with our previous stability discussions. In addition to this, note that the coating interface begins to take on a wavelength that is comparable to the wavelength prediction of Sec. IV C. However, in Fig. 10, the coating does not become smooth like the results in Fig. 9. This difference may be caused by the period of the initial condition being twice as large in Fig. 10 than in Fig. 9. Hence, the longer wavelength structure persists consistent with the stability predictions.

Next we examine the evolution of initial coatings with rectangular trenches. Shapes such as these may be found in small-scale electronic applications.[8] These solutions are displayed in Figs. 11 and 12. Here we examine the role of the surface diffusion mechanism by varying $\psi_s D_s$ from 6.5×10^2 nm^3/s in Fig. 11 to 6.5×10^1 nm^3/s in Fig. 12.

For smaller values of $\psi_s D_s$ we see in Fig. 11 that the coating becomes multivalued in the $\hat{z}$ coordinate. For larger values of $\psi_s D_s$ this is not the case due to surface diffusion and etching dominating the deposition of coating material. Further as the surface diffusion in Fig. 12 decreases, the sharp corners of the coating remain.

In Figs. 11 and 12, it is important to note that the peaks grow faster than the valleys. With all other growth factors equal, this is due to the sharp increase in concentration as the

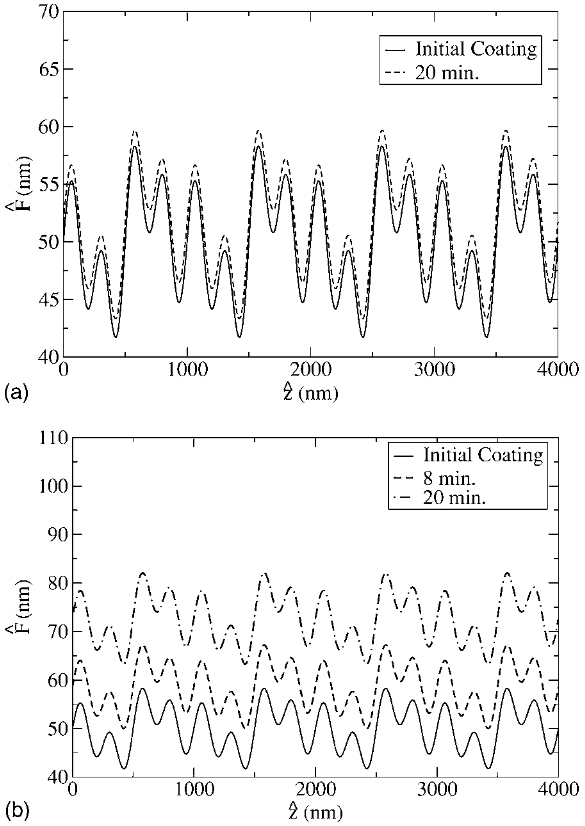

FIG. 10. Dimensional axial plot of the coated fiber ($k_F=7.5\times10^{11}\frac{\text{nm}}{\text{s}}$, $\hat{L}_F=4000$ nm, $\hat{S}_F=75$ nm). (a) $C^*=3\times10^{-37}\frac{\text{mole}}{\text{nm}^3}$. (b) $C^*=3\times10^{-36}\frac{\text{mole}}{\text{nm}^3}$.

radius of the fiber increases. Thus, peaks will grow quicker than valleys and larger bumps will grow quicker than smaller bumps.

In each of the above solutions the finger-like growth that is seen in other results[8,11,12] does not occur. This could be due to many different qualitative properties of this model. First, surface diffusion appears to significantly influence the coating process while it appears to have limited effect in other work.[8,11,12] This difference is likely due to the length scale at which growth is considered. The length scales of Refs. 8 and 11 are much larger than the scales presented here. This may result in surface diffusion playing a more prominent role. This phenomenon has been considered in Ref. 14. That investigation demonstrated that when the surface features of the coating are much shorter than the mean free path of the gas, that the surface diffusion and desorption of the adsorbate play a critical role in the coating morphology.

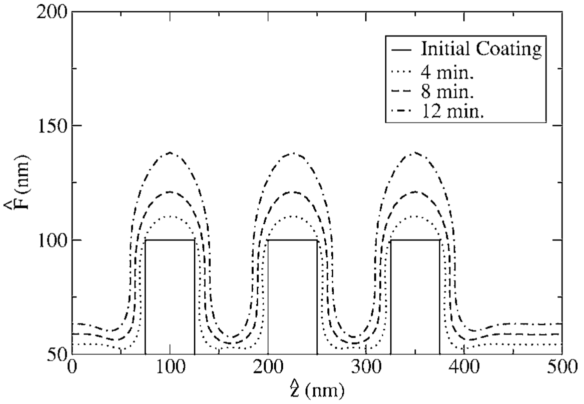

FIG. 11. Dimensional axial plot of the coated fiber ($C^*=3\times10^{-36}\frac{\text{mole}}{\text{nm}^3}$, $k_F=7.5\times10^{11}\frac{\text{nm}}{\text{s}}$, $\hat{L}_F=500$ nm, $\hat{S}_F=75$ nm, $\psi_s D_s=6.5\times10^{2}\frac{\text{nm}^3}{\text{s}}$).

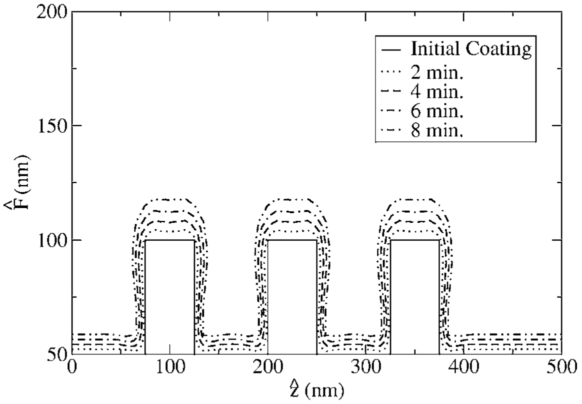

FIG. 12. Dimensional axial plot of the coated fiber ($C^*=3\times10^{-36}\frac{\text{mole}}{\text{nm}^3}$, $k_F=7.5\times10^{11}\frac{\text{nm}}{\text{s}}$, $\hat{L}_F=500$ nm, $\hat{S}_F=75$ nm, $\psi_s D_s=6.5\times10^{1}\frac{\text{nm}^3}{\text{s}}$).

Another reason finger-like growth may not occur is due to the method in which concentration is determined. As mentioned, the concentration model at the coating surface neglects large variations in the axial coordinate. Hence, some features of the concentration profile may not be captured in the simulations. For example, in the valleys of the coating in Fig. 11, as the coating first develops a mushroom-type shape, the pinching together of the peaks may result in a further reduction of concentration in the valleys. This would cause the peaks to grow faster than the valleys and a finger-like formation may occur as a result. This phenomenon, known as self-shadowing, has also been considered by Ref. 14 through the inclusion of relevant view factors for the impinging concentration flux over the surface. The concentration solution, Eq. (18), does not account for self-shadowing. In order to include self-shadowing, the full form of the concentration diffusion problem for transport of species to the coating surface should be solved numerically and iteratively with the evolution equation for the location of the coating free surface, similar to Refs. 8, 11, and 12. Additionally, one needs to further investigate the influence of nonsmooth coating surfaces on the MD simulations used to obtain the reaction and desorption coefficients k_F and k_{Fions}.

VI. SUMMARY

This article is part of a series[1,2] that addresses the modeling of coating growth onto nanofibers in a plasma enhanced physical vapor deposition (PEPVD) system. The overall goal of the effort is to develop a comprehensive model that connects various macroscale phenomena to nanoscale phenomena by linking simpler models at each length scale.

The present work uses all of the reactor scale information determined in Part I,[1] and all of the atomic scale information (provided by MD simulations that study the sputtering and deposition mechanisms at a curved nanoscale surface) determined in Part II.[2] This article, like Part II, focuses on the local nanofiber scale and investigates the interrelationships among processing factors for the transport and deposition of the coating material. As mentioned, Part II presents a local model defining nonuniform radial growth with uniform axial growth. The present work considers a model for uniform radial coating growth with nonuniform axial growth. The latter geometry is more consistent with observable and measurable experimental results.

Similar to Part II an evolution equation approach is used. Asymptotic solutions are used to reduce the complex model for concentration transport and deposition to a manageable, but still relevant, solution. In this procedure, derivatives in the axial direction are discarded in the concentration solution. Hence, a weakly nonlinear evolution equation is developed. This equation is linearized by assuming that the coating can be represented as the initial fiber radius plus small deposition bumps. This allows us to classify stabilizing terms as those that cause deposition and diffusion to the valleys of the coating and destabilizing terms as those that cause deposition and diffusion to the peaks of the coating. The linearized system is also solved to quantify the stability characteristics of the coating surface. In general the axial wavelength and magnitude of the coating roughness is larger for larger diameter fibers.

Additionally, the evolution equation is solved numerically using an arc-length parametrization technique. Numerical results indicate a high sensitivity of the coating morphology to the strength of the surface diffusion. Further it was found that coating growth increases as the reaction coefficient k_F increases. Increasing k_F results in an increase in deposition compared to surface diffusion. The coating growth also increases when the concentration of the neutral species at the reactor scale, C^*, is increased. Finally, with all other factors equal, peaks tend to grow faster than valleys due to the increased concentration levels at higher radial values.

Future work includes developing a model for three-dimensional deposition. Another extension to this model is considering deposition onto the bare fiber. This includes nucleation, island formation, and island growth of the deposited material. These processes are very complicated and must be investigated in order to develop a complete model. Finally, the full form of the concentration diffusion problem for transport of species to the coating surface should be solved numerically and iteratively with the evolution equation for the location of the coating free surface.

ACKNOWLEDGMENTS

This work was supported by NSF Grant No. DMI-0403835, and NASA Grant No. NNC04GB27G.

[1] A. Buldum, I. Busuladzic, C. B. Clemons, L. H. Dill, K. L. Kreider, G. W. Young, E. A. Evans, G. Zhang, S. I. Hariharan, and W. Keifer, J. Appl. Phys. **98**, 044303 (2005).
[2] A. Buldum, C. B. Clemons, L. H. Dill, K. L. Kreider, G. W. Young, X. Zheng, E. A. Evans, G. Zhang, and S. I. Hariharan, J. Appl. Phys. **98**, 044304 (2005).
[3] W. Liu, M. Graham, E. A. Evans, and D. H. Reneker, J. Mater. Res. **17**, 3206 (2002).
[4] A. L. Yarin, S. Koombhongse, and D. H. Reneker, J. Appl. Phys. **90**, 4836 (2001).
[5] A. L. Yarin, S. Koombhongse, and D. H. Reneker, J. Appl. Phys. **89**, 3018 (2001).
[6] D. J. Economou and R. C. Alkire, J. Electrochem. Soc. **135**, 2786 (1988).
[7] M. Gegick and G. W. Young, SIAM J. Appl. Math. **54**, 877 (1994).
[8] J. Thiart and V. Hlavacek, AIChE J. **41**, 1926 (1995).
[9] O. A. Louchev and Y. Sato, J. Appl. Phys. **84**, 6673 (1998).
[10] S. Osher and J. A. Sethian, J. Comput. Phys. **79**, 12 (1988).
[11] J. Thiart and V. Hlavacek, J. Comput. Phys. **125**, 262 (1996).
[12] G. S. Bales, A. C. Redfield, and A. Zangwill, Phys. Rev. Lett. **62**, 776 (1989).
[13] C.-W. Shu and S. Osher, J. Comput. Phys. **77**, 439 (1988).
[14] O. A. Louchev, Y. Sato, and H. Kanda, J. Appl. Phys. **89**, 2151 (2001).
[15] G. Zhang, Doctoral Dissertation, The University of Akron (2004).